Evaluating Land Subsidence Triggered by the 7.8 Mw Turkey-Syria Earthquake Using an Advanced Machine Learning Model

Ratiranjan Jena[1*], Abdallah Shanableh[1,2], Rami Al-Ruzouq[1,2]
Mohammed Barakat A. Gibril[1], Nezar Attala Hammouri[1], Ahmed Elawady[1], Hani Shanableh[1]

[1] GIS & Remote Sensing Center, Research Institute of Sciences and Engineering, University of Sharjah, Sharjah 27272, UAE; rjena@sharjah.ac.ae (R.J.); mbgibril@sharjah.ac.ae (M.B.A.G.); nhammouri@sharjah.ac.ae (N.A.H); aelawady@sharjah.ac.ae (A.E.); u20100583@sharjah.ac.ae (H.S.)

[2] Civil and Environmental Engineering Department, University of Sharjah, Sharjah 27272, UAE; shanableh@sharjah.ac.ae (A.S.); ralruzouq@sharjah.ac.ae (R.A.R.)

Keywords: Land Subsidence; Surface Deformation; Susceptibility; Turkey-Syria Earthquake; Extreme Learning Machine.

Abstract

The 7.8 M_w Turkey-Syria earthquake of 2023 caused massive destruction in several cities near the earthquake epicenter. However, there is a potential for significant land subsidence to occur across a broader region. Land subsidence, which can lead to significant infrastructure damage and ground deformation, necessitates detailed investigation. This research uses an advanced machine-learning technique to analyze the spatial distribution of earthquake-induced land subsidence and the extent of surface deformation. Sentinel-1 Synthetic Aperture Radar (SAR) data were processed to detect surface deformation near the epicenter and quantify the affected region's vertical displacement. An extreme learning machine model was developed using nine parameters, including slope, curvature, sediment thickness, soil thickness on slopes, peak ground acceleration, hydrologic soil, Vs30, land cover, and landslide probability. The model accurately predicted land subsidence susceptibility (accuracy of 85%) established correlations with ground deformation and observed vertical displacement. The results demonstrate that the deformation phase value ranges between 2.66 to -2.63, and the vertical displacement analysis suggests that a large portion of areas subsided downward up to 75 cm. Effectiveness of extreme learning machine in rapid land subsidence assessment, providing critical insights for disaster response and urban planning in seismically active areas. This study offers a useful solution for post-earthquake land subsidence analysis and lays the groundwork for integrating artificial intelligence with land subsidence research.

1. Introduction

Land subsidence is a significant geohazard, induced by various factors, including seismic activities, groundwater extraction, mining, and natural compaction processes, resulting in adverse effects on agriculture, water resources, and infrastructure. The 7.8 Mw earthquake that struck the Turkey-Syria border on February 6th, 2023, serves as a potential catalyst for severe ground deformation and land subsidence in the affected region (Li et al., 2023).

Traditional techniques for mapping and monitoring ground deformation, such as geotechnical surveys and field measurements, are limited, time-consuming, and labor-intensive. The advancement of remote sensing technologies, particularly Interferometric Synthetic Aperture Radar (InSAR), has been considered useful for detecting large-scale ground deformations (Ramirez et al., 2020). However, this technique faces challenges when analyzing complex ground displacement patterns located in areas having dense populations and vegetation. To address these challenges, the use of advanced machine learning models offers a promising solution for automated land subsidence analysis.

Existing studies have explored various aspects of land subsidence and ground deformation using remote sensing. Liu et al. (2024) proposed a spatiotemporal correlation analysis technique applying Independent Component Analysis (ICA) to extract multi-track deformation components and accurately retrieve earthquake deformation time series. Their approach was validated by comparing their results with data from three GPS stations, demonstrating that their approach produced smoother outcomes more closely aligned with GPS observations. Zhang et al. (2024) extracted and analyzed the coseismic deformation field based on pre-earthquake and post-earthquake Lutan-1 SAR data. The experimental results indicated effective deformation monitoring. The coseismic ruptures during the earthquake doublet were mostly left-lateral strike-slip movements. The maximum displacement in the North and East Anatolian fault zones reached 3.5 meters. These results demonstrated the ability of Lutan-1 SAR data for quantitative earthquake monitoring applications. In another study, Nofl et al. (2024) analyzed the surface deformation triggered by the February 6, 2023, earthquake along the Turkish-Syrian border, utilizing Sentinel-1 SAR data and Differential Interferometric Synthetic Aperture Radar (DInSAR) techniques. Their analysis identified distinct surface displacement patterns in northwest Syria and southern Turkey, with combined horizontal and vertical displacements of ±3.7 cm. Wang et al. (2024) presented coseismic deformation and surface displacements associated with the 2023 Türkiye-Syria Earthquake Doublet using SAR offset tracking measurements. Later, they inverted coseismic slip distributions, revealing a maximum fault slip exceeding 8 meters (Mw 7.8). In addition, Gkougkoustamos et al. (2023) conducted a study on the correlation of infrastructure exposure with ground deformation in Gaziantep and Kahramanmaraş cities using Sentinel-2 data and the Normalized Cross Correlation algorithm. Their results showed that displacements occurred from 5.4 m eastward to 2.8 m westward, while northward movement ranged up to 5.5 m, with some areas shifted southward up to 6.9 m. Alesheikh et al.

(2024) conducted a study that used the quasi-permanent scatterer method using the data (2018–2020) to detect subsidence and analyzed 12 geospatial factors to identify land subsidence susceptibility areas. Several ensemble approaches were implemented, such as adaptive-network-based fuzzy inference system (ANFIS) and ANFIS- particle swarm optimization (PSO), where ANFIS-PSO achieved a higher area under the curve (0.863) than ANFIS (0.771) on the test dataset. Zhang et al. (2023) conducted a subsidence study using 14 conditioning factors derived from geology, hydrology, topography, and human-induced activities, selected by conducting the multi-collinearity test. The result showed that the optimization models Bat optimization (BA) and Grey Wolf optimizer (GWO) were better than the other machine learning algorithms. However, limited research has focused on land subsidence linked explicitly to this seismic event at the Turkey-Syria border. A precise and timely evaluation of earthquake-induced land subsidence is essential for comprehending the extent of ground deformation and assessing the risk of future damage, which could facilitate the development of effective mitigation strategies. The existing research used traditional and ensemble machine learning approaches; however, it lacks the implementation of an advanced machine learning model. This paper aims to detect the extent of ground deformation, identify the subsidence zones, and generate a susceptibility map of land subsidence to understand the possibility of spatial distribution and intensity of land subsidence originating due to the 7.8 Mw Turkey-Syria earthquake. The study implemented an advanced machine learning-based framework for the susceptibility map generation. The study detects subsidence patterns and quantifies subsidence susceptibility by leveraging SAR imagery, conditioning factors, and an extreme learning machine model. Some of the methods of susceptibility mapping for other natural hazards, such as flood (Habibi et al. 2023) and earthquake (Jena et al. 2023), incorporate machine learning models and have shown promising results. The outputs of the vertical displacement of land and the ground deformation zones were correlated with the susceptibility map to validate the results. This study provides valuable information on understanding how seismic activity could trigger land subsidence and emphasizes the potential use of advanced machine learning techniques in analyzing post-earthquake hazards.

The rest of this manuscript is structured as follows: Section 2 presents the study area. Section 3 discusses the data used for this study. Section 4 describes the methodology, detailing the use of InSAR techniques for detecting ground deformation and an advanced machine learning model employed for subsidence susceptibility analysis. Section 5 presents the results, including ground deformation patterns, vertical displacement analysis, and subsidence susceptibility mapping. Section 6 discusses the implications of the findings. Finally, Section 7 summarizes the key conclusions and highlights potential areas for future research.

2. Study area

On February 6, 2023, a 7.8 Mw earthquake struck Gaziantep Province in Turkey (Figure 1). The epicenter of this earthquake was located at a focal depth of 17.5 km, near the surface outcrop of the East Anatolian Fault Zone (EAFZ). The EAFZ, which lies between the Arabian plate and the Anatolian plateau, is recognized as one of the most seismically active transform fault zones globally (Gürsoy et al., 2003; Khalifa et al., 2018). This earthquake led to numerous fatalities, rendering it the deadliest earthquake in Turkish history (Zhao et al., 2023). The Arabian tectonic block exerts pressure on the North Anatolian block to the northwest, causing the Anatolian plate to shift westward along the North Anatolian Fault Zone (NAFZ) (Reilinger et al., 2006; Emre et al., 2021). The fault zones experience variable slip rates due to the presence of conjugate fractures, pull-apart basins, and discontinuities. The region's geology is characterized by Paleozoic to Mesozoic metamorphic rocks, Mesozoic ophiolitic mélange, and volcanic formations (Hempton, 1985), which have been affected by the Early-Tertiary closure of the Neotethys Ocean and the southward movement of ophiolites over the Arabian foreland (Duman and Emre, 2013). The EAFZ also includes the Karasu Rift transition zone, marked by active faulting, basaltic volcanic activity, and sediment accumulation during the Quaternary period. The valley, bounded by the Amanos Mountains to the west and the Kurt Mountains to the east, is primarily filled with fluvial and lacustrine deposits mixed with volcanic material. To the southwest, the Karasu Rift connects with the Amik Basin, which lies at the intersection of the Asi Valley to the south and the Antakya-Samandag Corridor.

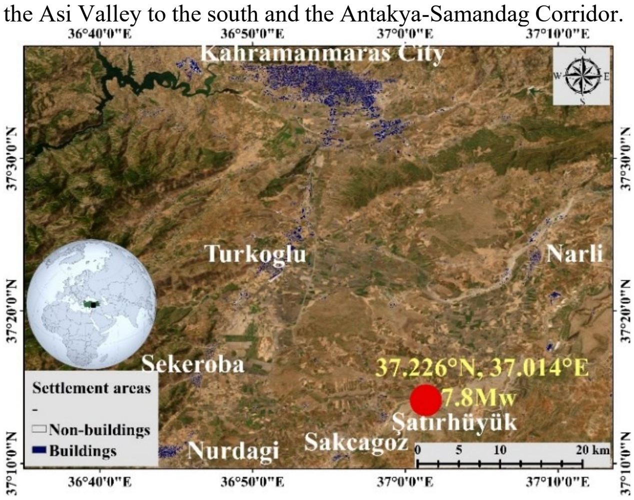

Figure 1. Study area.

3. Data

Several datasets were used in this analysis collected from various sources. The earthquake event of 7.8 Mw was sourced from the Latest Earthquake USGS. Peak ground acceleration (PGA) data was retrieved from the Humanitarian Data Exchange. Sentinel-1 data is known for its all-weather penetrated SAR imagery, which is most effective in detecting ground deformation and land subsidence. Sediment thickness, Soil thickness in slope, and hydrologic soil data were also implemented in this study collected from the Distributed Active Archive Center for Biogeochemical Dynamics. These datasets offer the conditioning factors that could influence the land subsidence geohazards. The shear-wave velocity at the top 30 meters of the soil (Vs30) was utilized along with a digital elevation model (DEM) obtained from the USGS Earth Explorer. Collection of datasets from various open sources, such as Sentinel-1, Landsat, and historical data, involves spatial resolution alignment, pre-processed by correcting for geometric, radiometric, and temporal differences, and using techniques such as resampling, coregistration, and data fusion to maintain consistency and reduce uncertainties. Table 1 provides a detailed summary of the datasets utilized for the extraction of damaged buildings and their spatial characteristics are shown in Figure 2.

Data	Factor	Spatial/Temporal Resolution	References
SAR imagery	Ground deformation	5 × 20 m, 6 days	Zhang et al., 2015)

Landsat-8	Landcover	30m, 16 days	(Babaee et al., 2024)
Vs30	Vs30 at the top 30m of the surface	1:250,000, Static	(Sairam et al., 2019)
PGA	Peak Ground Acceleration	1:250,000,	(Bardet et al., 2002)
Soil data	Sediment thickness, Soil thickness on slope, Hydrologic soil	1:250,000, based on historical data	(Ross et al., 2018)
DEM	Slope Curvature, 1-5 years	1:250,000	(Pirasteh et al., 2020)

Table 1. Summary of datasets used.

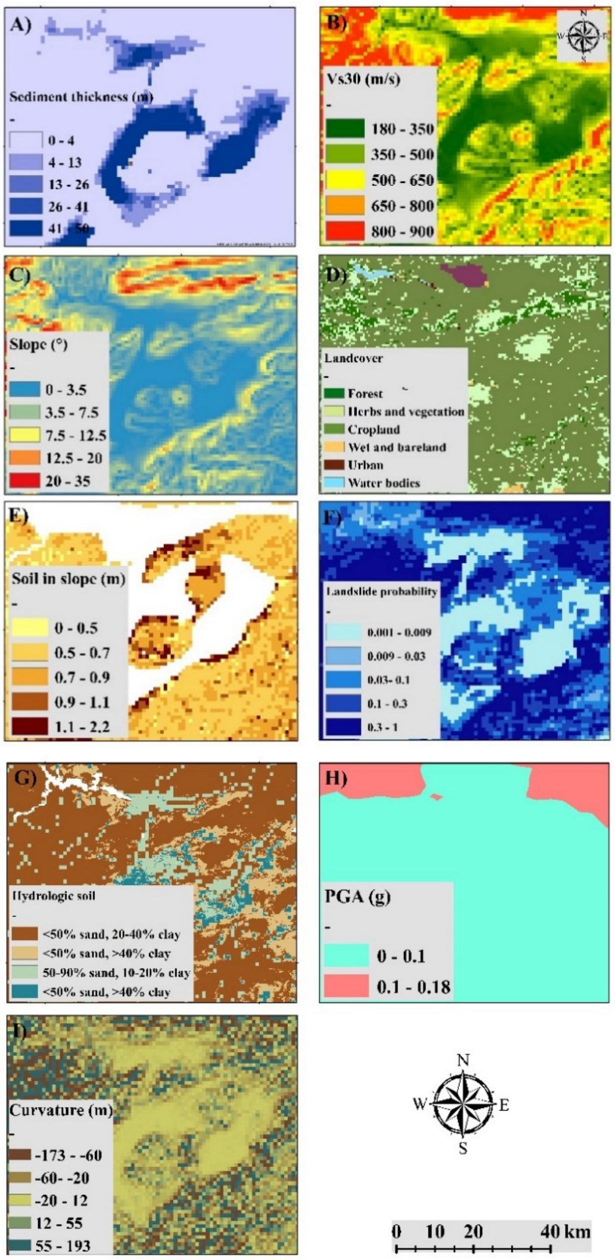

Figure 2. Conditioning factors used for the land subsidence assessment.

4. Methodology

4.1 Overall methodology

This study employed an InSAR technique based on the Sentinel Application Platform (SNAP) software to generate a ground deformation map (Figure 3). Prior to applying the InSAR technique for identifying deformed zones, the Sentinel-1 data underwent comprehensive preprocessing (Ramirez et al. 2020). Specifically, pre- and post-earthquake images dated February 4th and February 28th, 2023, respectively, were selected for analysis. These images were registered using the TOPSAR split function, alongside the application of orbit files to ensure precise orbit information. Techniques such as back-geocoding and enhanced spectral diversity were implemented to enhance data quality further, allowing images to be stacked within a unified geographic coordinate system. Subsequently, interferogram formation was conducted, and the TOPSAR Deburst technique was employed to merge individual images into a cohesive dataset. Topographic phase removal and Goldstein phase filtering were applied to improve the integrity of the InSAR-derived deformation zones to eliminate topographic effects and reduce noise within the phase data. A subset of the collected images was extracted to concentrate on the specific study area, thereby optimizing processing efficiency. Terrain correction was subsequently applied to accurately align with its corresponding position on the Earth's surface. The resulting data exhibited a clear representation of ground deformation. In a subsequent analysis focusing on vertical displacement mapping, a multilooking technique was implemented after the removal of the topographic phase. Additionally, Goldstein Phase Filtering was reapplied to diminish speckle noise further. The SANPHU unwrapping method was employed to estimate displacement across the study area, which encompasses urban regions, agricultural land, and barren areas that delineate the deformation zones. The findings from the vertical displacement mapping provided valuable insights into land subsidence features, facilitating further analysis. Selected points from the identified displaced locations were utilized to train an advanced machine-learning model. Furthermore, this study aimed to predict areas susceptible to land subsidence by considering nine conditioning factors.

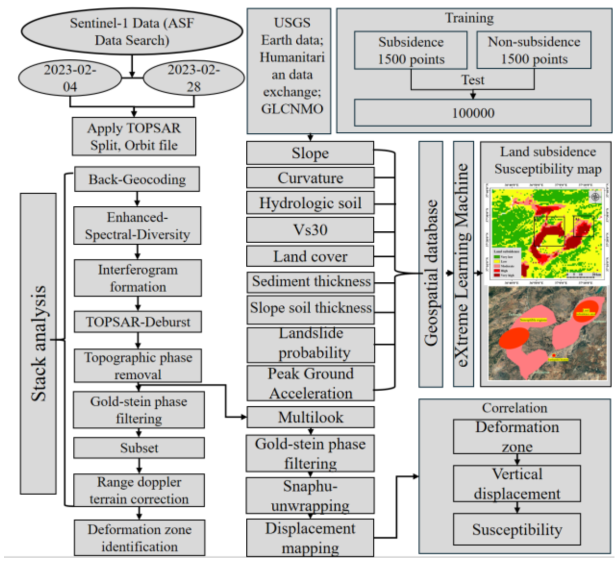

Figure 3. Methodological flowchart for the land subsidence assessment.

4.2 Extreme learning machine

An extreme learning machine (ELM) is a feed-forward network whose architecture matches the multi-layer perceptron (Figure 4). However, the hidden layer parameters in an ELM model are randomly generated and remain constant rather than being updated (Kannadasan et al. 2021). In the ELM model architecture, the hidden neurons are placed in the central, whereas the left and right side contains input and output, as demonstrated in Figure 4. There are n number of input vectors that can be classified using binary classification techniques named 1 and 0 output classes using L hidden neurons. The hidden layer neurons can be represented as $h(x) = [h_1(x), \dots\dots, h_L(x)]$. The significance of ELM hidden layers is that each hidden neuron in the layer conducts a nonlinear feature mapping generated from input neurons through the weight and bias as presented below.

$$\sum_{j=1}^{L} \beta_j g\left(w_j x_i + b_j\right) = O_i,\ \ i = 1,2 \dots .n \tag{1}$$

where X_i is the input feature, O_i is the output vector, w_j stands as the contribution amount of ith input to jth hidden neuron, where the bias is denoted as b, and the weights among the hidden neuron j and output class c is represented as $\beta_j = [\beta_1, .. \beta_C]^T$.

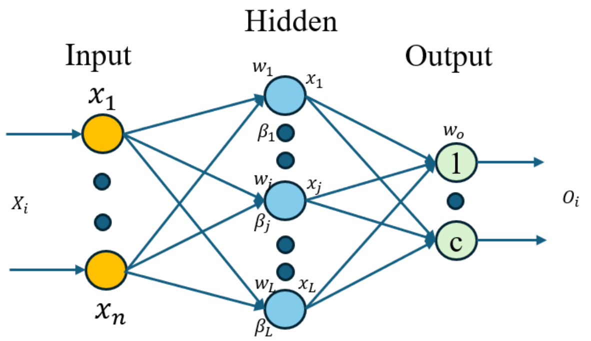

Figure 4. Architecture of the ELM model.

5. Results

5.1 Deformation zone

The ground deformation zone mapping methodology was implemented, as shown in Figure 3. The SAR single-pair images were pre-processed, and deformation zones were derived. Linear patterns indicate the fault movements or tectonic shifts in the zone. Irregular or distorted fringes suggest complex ground deformation patterns of surface subsidence, which could be due to landslides, seismic or mining activities. In this case, the pattern shows a seismic-based irregular pattern because of a 7.8 Mw earthquake. The map displays interference patterns due to phase differences between the SAR images captured at different times. A certain amount of displacement can be observed by each fringe, generally represented in millimeters or centimeters. In this case, the deformation is in phase, which is later changed to vertical displacement analysis with the exact value of displacement in centimeters. A cross-section named AB was plotted through the graph to understand the deformation condition along a line. Since the area is fully deformed, however, more deformation can be observed towards point A, whereas the deformation in the middle is less, and again, it's more towards point B. As illustrated in Figure 5, a large portion of the area is heavily deformed.

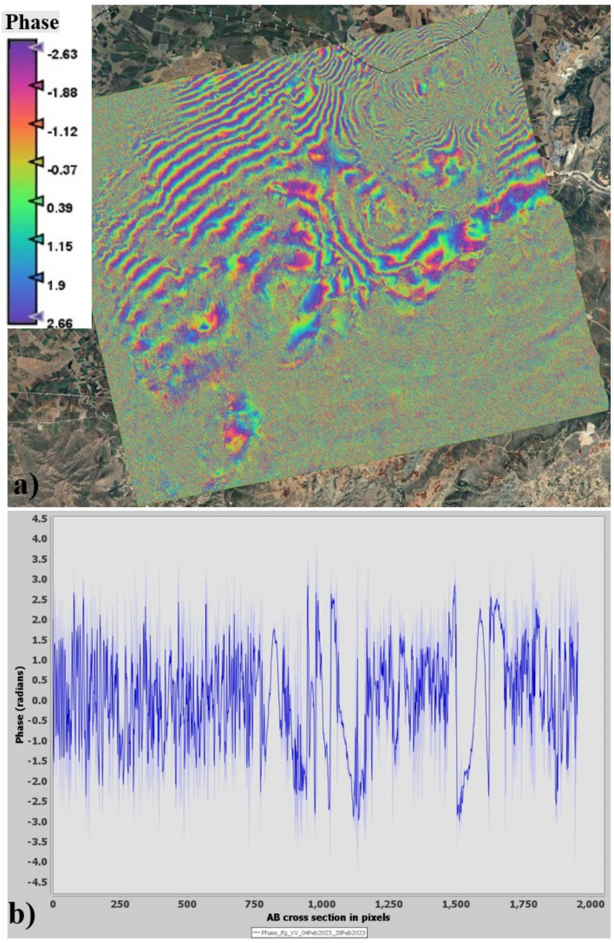

Figure 5. Deformation zone map for the area of interest. a) deformation zone map, b) AB cross section in the deformation zone.

5.2 Vertical displacement

A vertical displacement map was generated for the area of interest. The blue regions in the northwest sector of the study area indicate subsidence of approximately 75 cm, most likely caused by a high-magnitude earthquake of 7.8 Mw. In contrast, the central area represented through the yellow color remains stable with no significant displacement, as shown by the absence of fringes. The light yellow to dark green fringe is the transition zone between subsidence and the stable areas, representing a gradual change in ground displacement. The rate or magnitude of ground subsidence decreases progressively from the subsiding area towards the stable area. The graph below (Figure 6) shows a cross-section between points A and B. It can be clearly visible that the middle yellow portion is up while the blue areas on both sides are down due to subsidence. The atmospheric effects of land subsidence in this study were conducted by applying multi-temporal InSAR techniques to check and remove the noise using time series analysis. Empirical Mode Decomposition and interferogram stacking also help identify accurate surface displacement. This study shows a vertical displacement, which is validated using elevation data derived from InSAR, which did not exist before the earthquake. The results were also validated using a generated susceptibility map and tilting and liquefaction studies over the study area.

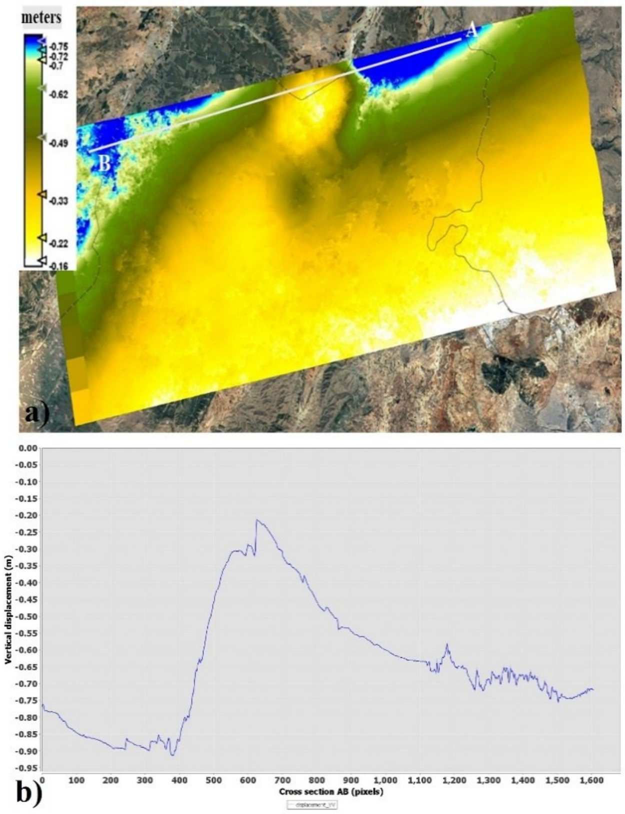

Figure 6. Vertical displacement zone map. a) vertical displacement map, b) AB cross section in the vertical displacement.

5.3 Land Subsidence Susceptibility

Land subsidence susceptibility assessment was conducted in the study area. According to the displacement map outputs, the study selected 3000 points for subsidence and non-subsidence areas based on the SNAP-based vertical displacement output. The developed eXtreme Learning Machine was implemented to predict the subsidence susceptibility. As per the obtained results, approximately 20% of the study is categorized as very high to moderate, and 80% as low to very low (Figure 7).

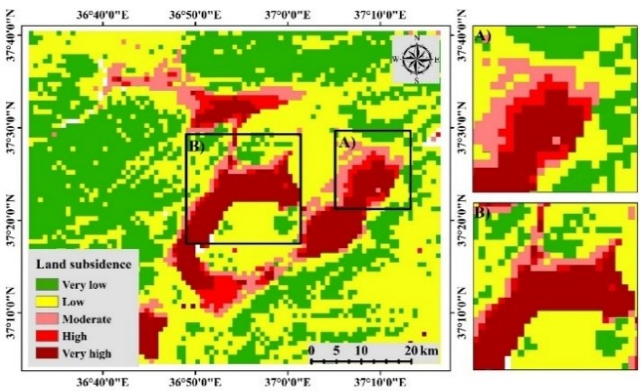

Figure 7. Land subsidence susceptibility map.

Some of the small cities named Turkoglu and Nurdagi are falling close to these highly susceptible zones. Due to this earthquake, several small buildings were demolished to the ground due to liquefaction, showing evidence of land subsidence. Those buildings located in small cities with high soil thicknesses and less runoff were affected. Kahramanmaras City was the most brutally affected one, with houses turning into ruins due to this earthquake, most probably due to several other reasons, however, not falling under the very high susceptibility zone of land subsidence. The selected study area has Vs30 values of 180 to 500 m/s, which is recorded in the central region, making it more susceptible to land subsidence. This earthquake greatly affected buildings, infrastructures, and transportation. Although the agricultural areas and some buildings fall under the very high susceptibility zone, not many were explicitly affected due to the land subsidence within the very high susceptibility zone.

6. Discussion

The 2023 Turkey earthquake, with a magnitude of 7.8 Mw, resulted in widespread destruction of buildings and infrastructure across the provinces of Adıyaman, Hatay, Kahramanmaraş, Gaziantep, Malatya, Şanlıurfa, Diyarbakır, Elazığ, and Adana. Preliminary assessments indicate that a significant portion of the observed damage can be attributed to geotechnical issues. Remote sensing and geospatial analyses provide further insights into the extent of the damage and potential underlying causes (Taftsoglou et al. 2023).

Toprak et al. (2023) reported lateral spreading and ground liquefaction events in Kahramanmaraş and Gaziantep following the 7.8 Mw Turkey-Syria earthquake. Field investigations and geospatial analysis reveal that cities like Gaziantep and Kahramanmaraş suffered severe damage, including tilting and toppling of structures, primarily due to the dynamic response of young alluvial soils with a high groundwater table. Therefore, groundwater depletion may not be the reason for land subsidence observed after the Kahramanmaras earthquake. However, soft soils, predominantly clay and sand, tend to amplify seismic waves, unlike hard rock formations that dampen them. The high proportion of soft soils in the central study area, primarily agricultural lands, corresponds to low Vs30 values, indicating high amplitude ground shaking. The area is characterized by young soil deposits and a high-water table and may have experienced land subsidence due to urbanization altering surface loading and subsurface conditions. Heavy infrastructure increased impervious surfaces, and seismic stress likely contributed to the loose soil compaction, causing such subsidence. The EAFZ experienced a peak slip exceeding 8 meters during the mainshock, with a rupture speed near the super-shear threshold (~1.5 m/s), contributing to significant land subsidence (Yu et al. 2024).

The deformation analysis indicates that regions with loose soil experienced greater deformation compared to those with hard rock. The presence of sand ejecta in exposed field areas further confirms soil instability and serves as evidence of land subsidence (Tobita et al. 2024). Vertical displacement analysis using SAR revealed that while the central part of the study area is characterized by stable ground conditions, the northeastern and northwestern regions exhibited significant soil failures. These findings underscore the necessity of a comprehensive assessment of soil properties and their geotechnical behavior for infrastructure planning and development. The area’s soil conditions suggest it is more suitable for agricultural use than for large-scale infrastructure projects. To ensure the safety and resilience of structures in seismically active regions, it is crucial to consider multiple factors, including slope, curvature, Vs30, hydrological soil properties, soil thickness, and sediment thickness.

The regions classified as having very high to moderate land subsidence susceptibility are characterized by low to moderate

Vs30 values, which tend to amplify seismic waves due to reduced shear wave velocity. Areas with low slopes and significant soil thickness are associated with loose soil conditions and reduced soil strength. Zones with very high susceptibility typically exhibit lower clay content (10-20%) and higher sand content (50-90%), creating a soil composition prone to liquefaction and extensive land subsidence. In contrast, moderate to low susceptibility regions occur when the sand content is below 50%, with silt and clay exceeding 35%, leading to lower overall soil stability and a reduced risk of severe subsidence. As shown in Figure 7, the central region of the study area is identified as a zone of very high susceptibility, which includes the districts of Gaziantep, Türkoğlu, Nurdağı, Şekeroba, Satırhüyük, and Bağlama, predominantly agricultural areas. This high susceptibility could potentially impact urban infrastructure located near these zones. The use of high-quality construction materials and robust building designs could mitigate the severity of damage in these regions. Building damage in the affected areas is not solely attributable to factors such as building height, soil thickness, liquefaction, and land subsidence; several structures along Malatya, Kahramanmaraş Yolu, Azerbaycan Boulevard, and Gazi Mustafa Kemal Boulevard were almost destroyed.

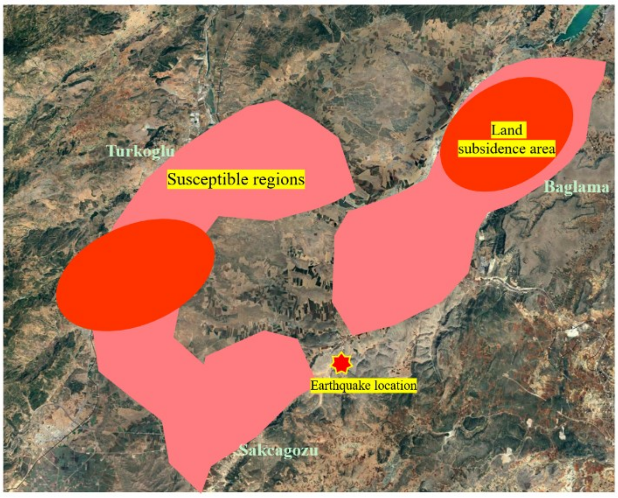

Figure 8. The Google Earth imagery overlaps land subsidence susceptibility and sentinel-based subsidence areas.

The proposed methodology exhibits high accuracy and efficiency by utilizing a three-dimensional framework for land subsidence analysis, which incorporates deformation zones, vertical displacement, and an advanced machine learning-based assessment of subsidence. The interaction between seismic and human-induced factors can make the interpretation difficult for susceptibility outputs and may reduce the accuracy and reliability by adding additional factors that affect ground deformation. The outputs of the model, presented in the form of a susceptibility map, were validated by correlating them with Google Earth imagery, deformation zones, and displacement maps. Validation results indicate that the land subsidence areas identified through detailed analysis of Sentinel-1 imagery align closely with the predicted susceptibility map (Figure 8). To verify the accuracy and reliability of the Sentinel-1 data and ground deformation maps, validation was conducted through cross-comparison with ground truth data, optical imagery, and published articles. Although the earthquake's epicenter is located near these susceptible zones, the actual subsidence was observed to occur slightly further from the epicenter.

7. Conclusions

This study utilized a SNAP-based interferometric technique to assess the deformation zone and vertical displacements resulting from the Gaziantep 7.8 Mw earthquake near the border of Türkiye-Syria. Analysis of these displacement changes provided helpful information regarding the fault ruptures and deformation characteristics. Additionally, an advanced machine learning model was implemented to assess the susceptibility of land subsidence. Finally, A correlation was then established between the deformation zone, displacement, and the susceptibility map. The significant observations from the study are concluded as follows: (1) The InSAR method observed the challenges owing to near-surface incoherence, whereas the InSAR-based vertical displacement method showcased the exact location of deformation and vertical displacement. (2) The deformation caused by the 7.8 Mw event caused several small-scale building damages but primarily impacted agricultural areas. Furthermore, the ascending data was used to derive the deformations, which resulted in excellent maps. (3) The 7.8 Mw earthquake mainly triggered the vertical displacement in the northeast and southwest parts of the southern EAFZ. (4) The vertical displacement zones fall under the very high to moderate susceptibility zone. These zones are characterized by low runoff and high soil thickness, low to moderate Vs30 (180-500 m/s), soil with 90 percent sand and less than 20% clay, and low slope. (5) The Mw 7.8 earthquake generated strong Coulomb stress, which is loaded in the Turkoglu Fault and could lead to further large-scale land subsidence. Future studies should consider further investigation of the land subsidence using geodetic techniques such as InSAR, combined with hydrogeological and geotechnical assessments, which is necessary to quantify the contribution of anthropogenic factors. In fact, long-term monitoring of land subsidence, considering the potential locations of future seismic events, is vital to understanding the ongoing risks. Therefore, long-term monitoring could significantly influence future infrastructure planning by adopting proper strategies and mitigating the subsidence impact in affected regions.

Acknowledgments

The authors sincerely thank the University of Sharjah for its invaluable support in enabling this research.

Conflicts of Interest

The authors declare no conflict of interest.

References

Alesheikh, A.A., Chatrsimab, Z., Rezaie, F., Lee, S., Jafari, A., Panahi, M., 2024. Land subsidence susceptibility mapping based on InSAR and a hybrid machine learning approach. *Egypt. J. Remote Sens. Space Sci.*, *27*(2), pp.255-267.

Babaee, S., Khalili, M.A., Chirico, R., Sorrentino, A., Di Martire, D., 2024. Spatiotemporal characterization of the subsidence and change detection in Tehran plain (Iran) using InSAR observations and Landsat 8 satellite imagery. *Remote Sens. Appl.: Soc. Environ.*, 36, p.101290.

Bardet, J.P., Tobita, T., Mace, N., Hu, J., 2002. Regional modeling of liquefaction-induced ground deformation. *Earthq. Spectra.*, 18(1), 19-46.

Duman, T.Y., Emre, Ö., 2013. The East Anatolian Fault: geometry, segmentation, and jog characteristics. *Geol. Soc. Spec. Publ.*, 372(1), 495-529.

Emre, Ö., Kondo, H., Özalp, S., Elmacı, H., 2021. Fault geometry, segmentation, and slip distribution associated with the 1939 Erzincan earthquake rupture along the North Anatolian fault, Turkey. GeoScienceWorld, London.

Gürsoy, H., Tatar, O., Piper, J., Heimann, A., Mesci, L., 2003. Neotectonic deformation linking the east Anatolian and Karataş-Osmaniye intracontinental transform fault zones in the Gulf of İskenderun, southern Turkey, deduced from paleomagnetic study of the Ceyhan-Osmaniye volcanics. *Tectonics*, 22.

Habibi, A., Delavar, M.R., Nazari, B., Pirasteh, S., Sadeghian, M.S., 2023. A novel approach for flood hazard assessment using hybridized ensemble models and feature selection algorithms. *Int. J. Appl. Earth Obs.*, *122*, p.103443.

Hempton, M.R., 1985. Structure and deformation history of the Bitlis suture near Lake Hazar, southeastern Turkey. *Geol. Soc. Am. Bull.*, 96(2), 233-243.

Jena, R., Pradhan, B., Gite, S., Alamri, A., Park, H.J., 2023. A new method to promptly evaluate spatial earthquake probability mapping using an explainable artificial intelligence (XAI) model. *Gondwana Res.*, *123*, pp.54-67.

Kannadasan, R., Alsharif, M.H., Jahid, A. Khan, M.A., 2021. Categorizing diseases from leaf images using a hybrid learning model. *Symmetry*, *13*(11), p.2073.

Khalifa, A., Çakır, Z., Owen, L., Kaya, S., 2018. Morphotectonic analysis of the East Anatolian Fault, Turkey. *Turk. J. Earth Sci.*, 27, 110-126.

Li, S., Wang, X., Tao, T., Zhu, Y., Qu, X., Li, Z., Huang, J., Song, S., 2023. Source model of the 2023 Turkey earthquake sequence imaged by Sentinel-1 and GPS measurements: Implications for heterogeneous fault behavior along the East Anatolian Fault Zone. *Remote Sens-Basel*, 15, p. 2618.

Liu, Y., Wu, S., Zhang, B., Xiong, S., Wang, C., 2024. Accurate Deformation Retrieval of the 2023 Turkey–Syria Earthquakes Using Multi-Track InSAR Data and a Spatio-Temporal Correlation Analysis with the ICA Method. *Remote Sens-Basel*, 16(17), p.3139.

Nofl, D., Darwishe, H., Chaaban, F., Mohammad, A., 2024. Mapping surface displacements after the 6 February 2023 earthquake in Syria and Turkey using DInSAR and GIS techniques. *Spat. Inf. Res*, 32(3), 231-251.

Ramirez, R., Lee, S., Kwon, T., 2020. Long-term remote monitoring of ground deformation using Sentinel-1 Interferometric Synthetic Aperture Radar (InSAR): Applications and insights into geotechnical engineering practices. *Appl. Sci.*, 10, p. 17447.

Reilinger, R., McClusky, S., Vernant, P., Lawrence, S., Ergintav, S., Cakmak, R., Ozener, H., Kadirov, F., Guliev, I., Stepanyan, R., Nadariya, M., 2006. GPS constraints on continental deformation in the Africa-Arabia-Eurasia continental collision zone and implications for the dynamics of plate interactions. *J. Geophys. Res-Sol. Ea.,* 111(B5).

Ross, C.W., Prihodko, L., Anchang, J., Kumar, S., Ji, W., Hanan, N.P., 2018. Global hydrologic soil groups (HYSOGs250m) for curve number-based runoff modeling. ORNL DAAC, Oak Ridge, Tennessee, USA.

Sairam, B., Singh, A.P., Patel, V., Chopra, S., Kumar, M.R., 2019. VS30 mapping and site characterization in the seismically active intraplate region of Western India: implications for risk mitigation. *Near Surf. Geophys.*, 17(5), 533-546.

Taftsoglou, M., Valkaniotis, S., Karantanellis, E., Goula, E., Papathanassiou, G., 2023. Preliminary mapping of liquefaction phenomena triggered by the February 6 2023 M7.7 earthquake, Türkiye/Syria, based on remote sensing data. *Zenodo*. DOI: 10.5281/zenodo.7668401.

Tobita, T., Kiyota, T., Torisu, S., Cinicioglu, O., Tonuk, G., Milev, N., Contreras, J., Contreras, O. Shiga, M., 2024. Geotechnical damage survey report on February 6, 2023 Turkey-Syria Earthquake, Turkey. *Soils Found.*, *64*(3), p.101463.

Toprak, S., Zulfikar, A.C., Mutlu, A., Tugsal, U.M., Nacaroglu, E., Karabulut, S., Ceylan, M., Ozdemir, K., Parlak, S., Dal, O., Karimzadeh, S., 2024. The aftermath of 2023 Kahramanmaras earthquakes: evaluation of strong motion data, geotechnical, building, and infrastructure issues. *Nat. Hazards*, 1-38.

Wang, W., Liu, Y., Fan, X., Ma, C., Shan, X., 2023. Coseismic Deformation, Fault Slip Distribution, and Coulomb Stress Perturbation of the 2023 Türkiye-Syria Earthquake Doublet Based on SAR Offset Tracking. *Remote Sens-Basel*, 15(23), p.5443.

Yu, X., Hu, X., Song, Y., Xu, S., Li, X., Song, X., Fan, X. and Wang, F., 2024. Intelligent assessment of building damage of 2023 Turkey-Syria Earthquake by multiple remote sensing approaches. *npj Nat. Hazards*, *1*(1), p.3.

Zhang, L., Arabameri, A., Santosh, M., Pal, S.C., 2023. Land subsidence susceptibility mapping: comparative assessment of the efficacy of the five models. *Environ. Sci. Pollut. R.*, *30*(31), pp.77830-77849.

Zhang, L., Ding, X., Lu, Z., 2015. Ground deformation mapping by fusion of multi-temporal interferometric synthetic aperture radar images: A review. *Int. J. Image Data Fus.*, 6(4), 289-313.

Zhang, X., Tang, X., Li, T., Zhao, H., Zhang, X., Lu, J., Lv, S., 2024, April. Turkey-Syria Mw 7.8 Earthquake Deformation Monitoring Using Lutan-1 SAR Data. In *2024 Photonics & Electromagnetics Research Symposium (PIERS),* 1-5. DOI: 10.1109/PIERS62282.2024.10618826.

Zhao, J.J., Chen, Q., Yang, Y.H., Xu, Q., 2023. Coseismic faulting model and post-seismic surface motion of the 2023 Turkey–Syria earthquake doublet revealed by InSAR and GPS measurements. *Remote Sens-Basel*, 15(13), p.3327.